Supplementary Materials for

In Situ Observations of Earthquake-Driven Fluid Pulses within the Japan Trench Plate Boundary Fault Zone

Fulton, P. M., E. E. Brodsky
correspondence to: pfulton@tamu.edu

This PDF file includes:

Materials and Methods:

Temperature Data

Temperature data were collected with 55 miniature temperature loggers (MTLs): 10 TDR-2050s and 15 TR-1050s manufactured by RBR Ltd. (Canada; **www.rbr-global.com/**) and 30 Antares 1357 high-pressure data loggers manufactured by Antares Datensysteme GmbH (Germany; **www.antares-geo.de/**). Each of the MTLs has an autonomous data logger and a temperature sensor enclosed within titanium casings pressure rated for up to 10,000 m water depth. The TDR-2050s also have a pressure sensor that effectively records the sensor's water depth inside the cased borehole. The MTLs were attached to spectra rope and wrapped with a rubber protective covering. The sensor string was attached to a hanger and hung within 3.5" steel tube casing with a check-valve at the bottom that prohibited fluids from flowing into the casing from below. Spacing between sensors varied from 1.5 m at the bottom near the fault zone to 3 m, 6 m and greater intervals higher up. The sensors recorded every 10s, 20s or 10 minutes depending upon the model. The RBR temperature sensors have a resolution of <0.00005°C and the Antares have a resolution of 0.001°C. In addition to factory calibration constants, each temperature sensor was calibrated using a Hart Scientific water bath containing a mixture of ethylene glycol and water and an NIST reference temperature probe over 8 or more different temperatures from 0 – 30^{o}C and spanning the range recorded during the JFAST experiment. The resulting sensor corrections permit accuracy for all temperature sensors to within ~0.001^{o}C. Reliable corrections were unable to be obtained for sensors at 745 and 805 mbsf. The absolute temperatures for these two sensors may be off by a several milliKelvin, although their residual temperatures appear consistent with neighboring data. A depth profile of the corrected temperature averaged for the day of 1 December 2012 is shown in Figure DR1. Additional details regarding the sensors and observatory are described in *Fulton et al.,* (2013) and *Chester et al.,* (2013b).

Residual Temperature

Calculation of residual temperature for this data was reported by *Fulton et al.* [2013] in which a background geotherm is computed and removed from the corrected temperature data. Based on least squares fits to the data, the assumed average background geotherm starts from a projected temperature at the sea floor of 2.50^{o}C and increases by 27.57 ^{o}C/km until 650 mbsf and then continues by 26.29^{o}C/km to the bottom of the sensor string.

Plotting

Because the spacing between sensors and the measurement duration for different sensors are not the same, the color maps for residual temperature and high-pass filtered temperature are plotted using nearest neighbor interpolation in the spatial dimension for illustrative purposes. The effect provides for better visual presentation of the data but has no direct influence on the interpretations or conclusions.

High-pass filter

To compare high-frequency signals on different sensors at different depths, we first down sample data from the sensors with high sampling rate so that data for subsequent analysis are synchronous in time and have a consistent sampling interval of 10 minutes.
The data are then trimmed in time to focus only on data starting from 15 September 2012 in order to avoid most of the early data that is largely affected by drilling disturbance. The data are then detrended and tapered to 5% of each side and high-pass filtered such that signals with periods longer than or equal to 20 days are removed. The choice of filter cut-off has very little effect on the results and is somewhat arbitrary. We choose 20 days because the characteristic recovery time for the drilling disturbance ranges from 21 to 50 days (Figure 2), and thus its effects are largely filtered out. Figure DR2A shows results for the period in which ocean bottom pressure data is also available from 6 October 2016 to 24 April 2016. Figure 3 shows the results for December 2012 when many transients are observed. Results utilizing an alternative high-pass filter with a period of 60 days as the cutoff period reveal very little difference when compared to Figures 3 and DR2.

Cross-correlation for finding advective signals

To assess whether temperature perturbations are correlated across different sensors at different depths, we compare the signal of each sensor to the neighboring sensor above. For each sensor we compute the normalized cross-correlation of detrended signals. For different time windows of either 6 hours or 48 hours we take the high-pass filtered data of the two sensors, detrend them both, and calculate the maximum normalized cross-correlation between the two. The choice of time window ranging from 6 to 48 hours is roughly based on the observed duration of transient disturbances visually identifiable within the filtered data (Figures 3 and DR2); larger time windows are more apt to capture signals with large lag times between sensors or long wavelengths, whereas shorter time windows provide greater temporal resolution.

The normalized cross-correlation of two vectors x and y is defined by:

$$x \bigstar y = R_m = \begin{cases} \dfrac{\sum_{n=1}^{N-m} x_{n+m}\,\overline{y_n}}{\sqrt{\sum_{n=1}^{N}|x_n|^2 \sum_{n=1}^{N}|y_n|^2}} & m \geq 0 \\ \dfrac{\sum_{n=1}^{N+m} x_n\,\overline{y_{n-m}}}{\sqrt{\sum_{n=1}^{N}|x_n|^2 \sum_{n=1}^{N}|y_n|^2}} & m < 0 \end{cases} \quad \text{(DR1)},$$

where the cross-correlation at a given time lag between the two signals τ is the sum of the products between corresponding components of x and the conjugate (denoted by the over-bar) of y. N is the number of samples within the evaluated time window, and the indexes of the vector components within that window range from 1 to N. Correlations are computed for different lags of m ranging $-N+1$ to $N-1$, corresponding to integer offsets in the component indexes between the two vectors. These offsets also correspond to time lags of $\tau = m\Delta t$, where Δt is the sampling rate interval of 10 minutes. The term in the

104 denominator of Equation DR1 normalizes the values so that the autocorrelations at zero
105 lag equal 1. The result of Equation 1 is a vector of correlation coefficient as a function of
106 lag between the two signals, R_m. We record the maximum correlation coefficient of all
107 allowable time lags for the prescribed window length and associate the result with the
108 start of the time window being considered. Progressively, the time window is advanced
109 one measurement time interval (10 minutes) into the future and the calculations are
110 performed again.
111
112 The cross-correlation is computed only for the sensors that recorded for long-periods of
113 time during the experiment. They are only calculated for the nearest relevant sensor
114 above and not for all potential sensor pairs. The associated depth for each calculation is
115 the mid-point between the sensors being evaluated. The results are values of maximum
116 correlation coefficient as a function of both depth and time. We focus our interpretations
117 on data at depths ≥650 mbsf where sensors are relatively closely spaced; most of the
118 anomalous signals in both the maps of high-filtered temperature and correlation
119 coefficient appear at depths ≥750 mbsf. The time focus of our analysis is between 6
120 October and 24 April 2013, when nearby ocean bottom pressure measurements are
121 available.
122
123 *Ocean-Bottom Pressure Data*
124 Data from a Tohoku University ocean-bottom pressure sensor (OBP) recorded data near
125 the JFAST observatory during the 9-month observatory experiment have been graciously
126 shared by Prof. Ryoto Hino. The OBP instrument recorded from 5 October 2012 to 24
127 April 2013 at a location of 37.93357^{o}N 143.91543^{o}E in a water depth 6482 m and
128 roughly within 1 km of the JFAST observatory. To isolate the ocean bottom pressure
129 response from earthquakes we have applied a 2-point running average and a high-pass
130 filter that removes periods longer than 30 seconds from the 1 Hz data. Large pressure
131 spikes due to earthquake ground motions are apparent in the filtered OBP data.
132
133 *Earthquakes*

We identify pressure spikes > 100 Pa in the OBP data and use the timing to identify the causal earthquake in the Japan Meteorological Agency (JMA) earthquake catalog (http://www.jma.go.jp). For far-field earthquakes we utilize the ANSS composite earthquake catalog (http://quake.geo.berkeley.edu/anss/). The resulting list of 71 earthquakes is shown in Table DR1.

Identification of earthquake-driven fluid pulses

For each of the 71 earthquakes identified in the OBP data, we queried the cross-correlation maps to assess whether there was evidence of the earthquake driving fluid advection. Advection signals indicative of transient fluid pulses were observed for 28 of the 71 earthquakes (Table DR1). We then compared characteristics of the earthquakes including the moment magnitude, great circle distance from the JFAST site, and magnitude of the absolute value of the OBP pressure spike to assess differences between earthquakes with fluid pulses and those without (Figures DR4 and DR5). Distances are computed as the great circle distance between the reported latitude and longitude of the earthquake point location and the latitude and longitude of the JFAST observatory at 37.9387^{o}N, 143.9133^{o}E. It is likely that the land-based JMA network has unusually large location errors for the largely near-trench events.

Earthquake focal mechanisms and static volumetric strain

To assess whether earthquakes identified as being associated with fluid pulses have a similar static strain effect at the JFAST site, we compute the expected volumetric strain direction of either compression or dilation at the JFAST based on the method of Okada, (1995). The method requires knowledge of the earthquake focal mechanisms which we obtained for the NIED Earthquake Focal Mechanism catalog (http://www.fnet.bosai.go.jp/event/search.php?LANG=en). Of the 71 earthquakes, 51 had focal mechanisms in this catalog. The results show no apparent correlation between volumetric strain direction and earthquakes with or without fluid pulses.

Numerical simulations

To assess whether the temperature observations are consistent with the interpretation of transient fluid flow into a borehole, we constructed a numerical model of fluid flow and heat transport to simulate transient fluid flow into the JFAST borehole annulus. The finite element model, constructed in Comsol, consists of a radially symmetric model domain representative of a 4.5" steel pipe in a 10" borehole surrounded by rock with varying permeability (Figure DR5). We model fluid flow as a transient response to an initial pore pressure within a permeable fracture zone that extends a finite radial distance away from the borehole. Pore pressure is allowed to diffuse following Darcy's law of fluid flow in a porous medium into the surrounding country rock or into the borehole annulus. Fluid flow in the annulus is assumed to be laminar flow for simplicity. Because the background temperature in the system follows the geothermal gradient, as fluids move up the borehole annulus they tend to warm the surroundings (and observatory sensors) and when they flow down they cool the surroundings. The results of a model simulation with a 10 m wide fracture zone with permeability of $3x10^{-13}$ m^2, a country rock permeability of 10^{-20} m^2, and an initial excess pore pressure of 25 kPa are shown in Figure 4A. The resulting relative temperature changes as a function of depth are consistent with the pattern of observed temperature changes following earthquakes (Figure 4).

Model results suggest that the temperature patterns are sensitive to both the fluid flow rate and its time evolution and do not uniquely constrain the permeability and initial pressure conditions. In addition to an initial excess pressure, P_o, and assumed fracture zone permeability, k_f, rapid decay of flow rate is controlled by the lateral radial extent, R, of the permeable overpressured zone. In reality, fluid flow rates are likely modulated by more complicated processes.

Figure DR6 shows results of simulations with different permeability, initial pressure, and radial extent of the permeable zone that result in different absolute peak fluid velocities (*max V*), yet all result in similar temperature patterns that resemble the observations. Figure DR7 shows examples of the sensitivity of model parameterization choices on resulting temperature patterns.

195

196 *Background fluid flow rates*

197 To assess the magnitude of possible background fluid flow rates we analyze the thermal
198 anomalies around 763 and 784 mbsf (Figure 2) which appear and disappear in response to
199 the 7 December 2012 event, respectively, and have previously been interpreted as a
200 change in the preferred flow path for background fluid flow. Assuming the rate of
201 temperature change is related to product of the change in vertical fluid flow rate and the
202 background temperature gradient of 26.29^{o}C km^{-1} (Fulton et al., 2013) the sudden ~0.1
203 ^{o}C change in persistent temperature values at these depths over the course of a month,
204 would suggest background fluid flow rates on the order of ~10^{-6} m/s.

205

206

FIGURE CAPTIONS

Figure DR1. Temperature-depth profile of the average corrected temperature on 1 December 2012.

Figure DR2. Similar to Figure 3. A) High-pass filtered temperature data (periods < 20 days) from depths 650-820 mbsf for the time period of 6 October 2012 to 24 April 2013 during which time nearby ocean bottom pressure (OBP) data were recorded. B) Earthquakes identified in OBP measurements and their magnitude. C) Correlation coefficient between neighboring sensors' high-pass filtered temperature data utilizing a 48 hour moving window. High correlation reveals where and when active fluid advection is occurring.

Figure DR3. Absolute magnitude of pressure spikes > 100 Pa caused by earthquakes in high-pass filtered ocean bottom pressure data. The instrument recorded data within less than 1 km from the JFAST observatory from 6 October 2012 to 24 April 2013. Earthquakes associated with fluid pulse signals in the temperature data are black and those not associated with fluid pulses are orange.

Figure DR4. Magnitude and great circle distance of earthquakes identified in ocean bottom pressure data from a nearby instrument. Distance is measured as the great circle distance from the JFAST observatory. Earthquakes associated with fluid pulse signals in the temperature data are black and those not associated with fluid pulses are orange.

Figure DR5: Schematic diagram of numerical model domain. Transient fluid flow and heat transport respond to an initial pore pressure within the permeable fracture zone P_o that is allowed to diffuse into the surrounding country rock or driving fluid flow into the borehole and up and down the annulus around the water-filled steel pipe observatory. Pressure continuity is maintained at the interface between the annulus and formation. Fluid is only allowed to escape the domain through the top and bottom of the borehole. Temperature boundary conditions at the top and bottom of the domain are consistent with

the geothermal gradient which also defines the initial linearly stratified temperature distribution.

Figure DR6: Similar to Figure 4, results of model simulations with different permeability k_f, initial pressure P_o, and radial extent of the permeable zone R, that result in different absolute peak fluid velocities (*max V*), yet all result in similar temperature patterns that resemble the observations. Panel A shows the same results as Figure 4A and Figure DR7C.

Figure DR7: Similar to Figure 4. Results of model simulations that together highlight the sensitivity of model parameterization choices on resulting temperature patterns. For the same fracture zone permeability, differences in either initial pressure P_o or radial extent of the permeable zone R affect the resulting pattern but do not necessarily affect the peak fluid velocity, *max v*. Panel C is the same result as Figure 4A and Figure DR6A.

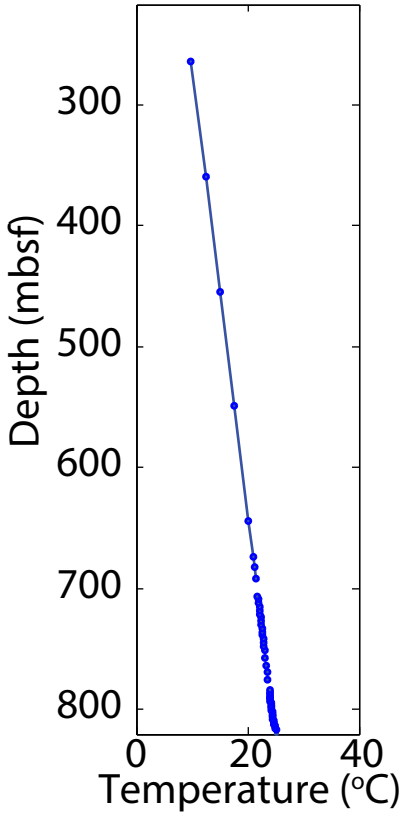

Figure DR1: Temperature-depth profile of the average corrected temperature on 1 December 2012.

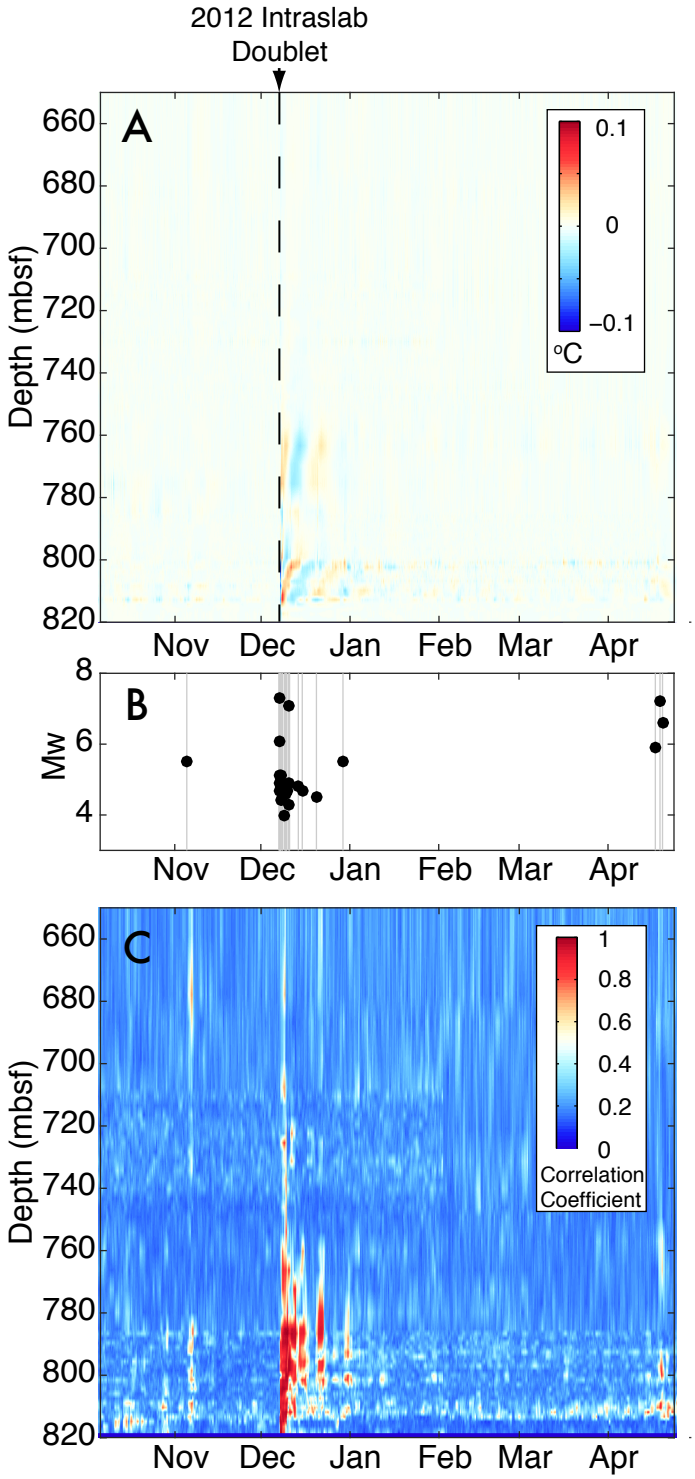

Figure DR2: A) High-pass filtered temperature data (periods < 20 days) from 6 Oct 2012 - 24 Apr 2013 and depths > 650 mbsf. B) Earthquakes identified in nearby ocean bottom pressure measurements and their magnitude. C) Correlation coefficient between neighboring sensors' high-pass filtered temperature data utilizing a 48 hour moving window. High correlation reveals where and when active fluid advection is occurring.

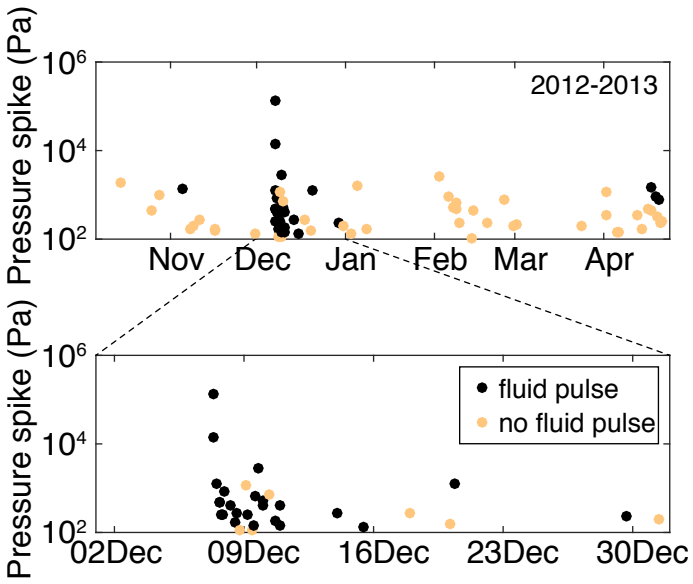

Figure DR3: Absolute magnitude of pressure spikes >100 Pa caused by earthquakes in high-pass filtered ocean bottom pressure data. The instrument recorded data within less than 1 km from the JFAST observatory from 6 October 2012 to 24 April 2013. Earthquakes associated with fluid pulse signals in the temperature data are black and those not associated with fluid pulses are orange.

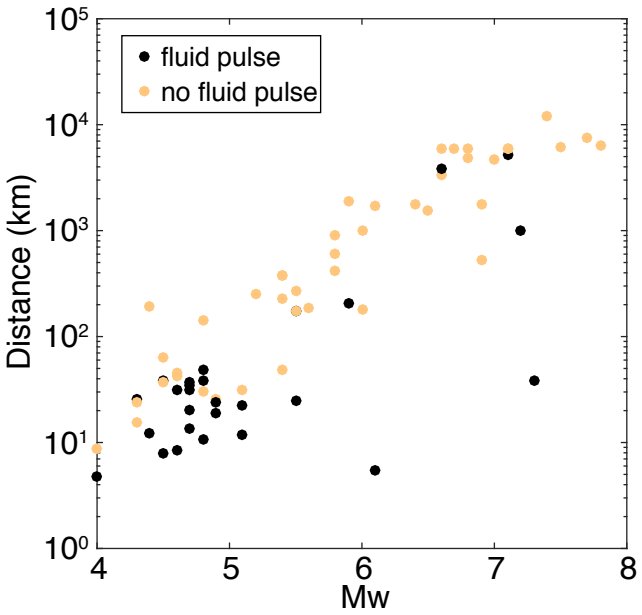

Figure DR4: Magnitude and great circle distance of earthquakes identified in ocean bottom pressure data from a nearby instrument. Distance is measured as the great circle distance from the JFAST observatory. Earthquakes associated with fluid pulse signals in the temperature data are black and those not associated with fluid pulses are orange.

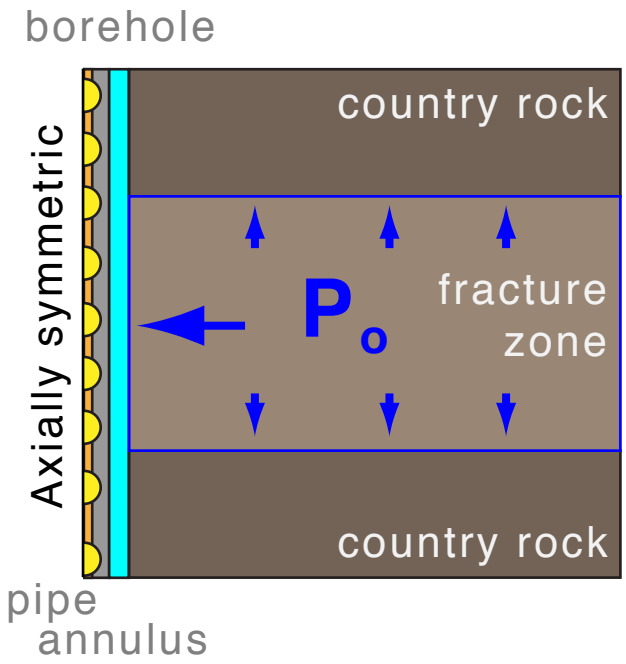

Figure DR5: Schematic diagram of numerical model domain. Transient fluid flow and heat transport respond to an initial pore pressure within the permeable fracture zone Po that is allowed to diffuse into the surrounding country rock or driving fluid flow into the borehole and up and down the annulus around the water-filled steel pipe observatory. Pressure continuity is maintained at the interface between the annulus and formation. Fluid is only allowed to escape the domain through the top and bottom of the borehole. Temperature boundary conditions at the top and bottom of the domain are consistent with the geothermal gradient which also defines the initial linearly stratified temperature distribution.

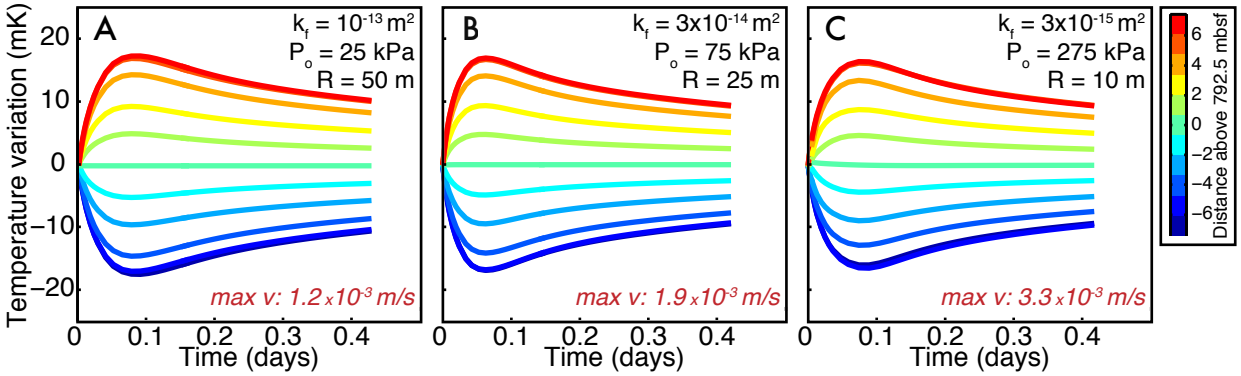

Figure DR6: Similar to Figure 4, results of model simulations with different permeability k_f, initial pressure P_o, and radial extent of the permeable zone R, that result in different absolute peak fluid velocities (max V), yet all result in similar temperature patterns that resemble the observations. Panel A shows the same results as Figure 4A and Figure DR7C.

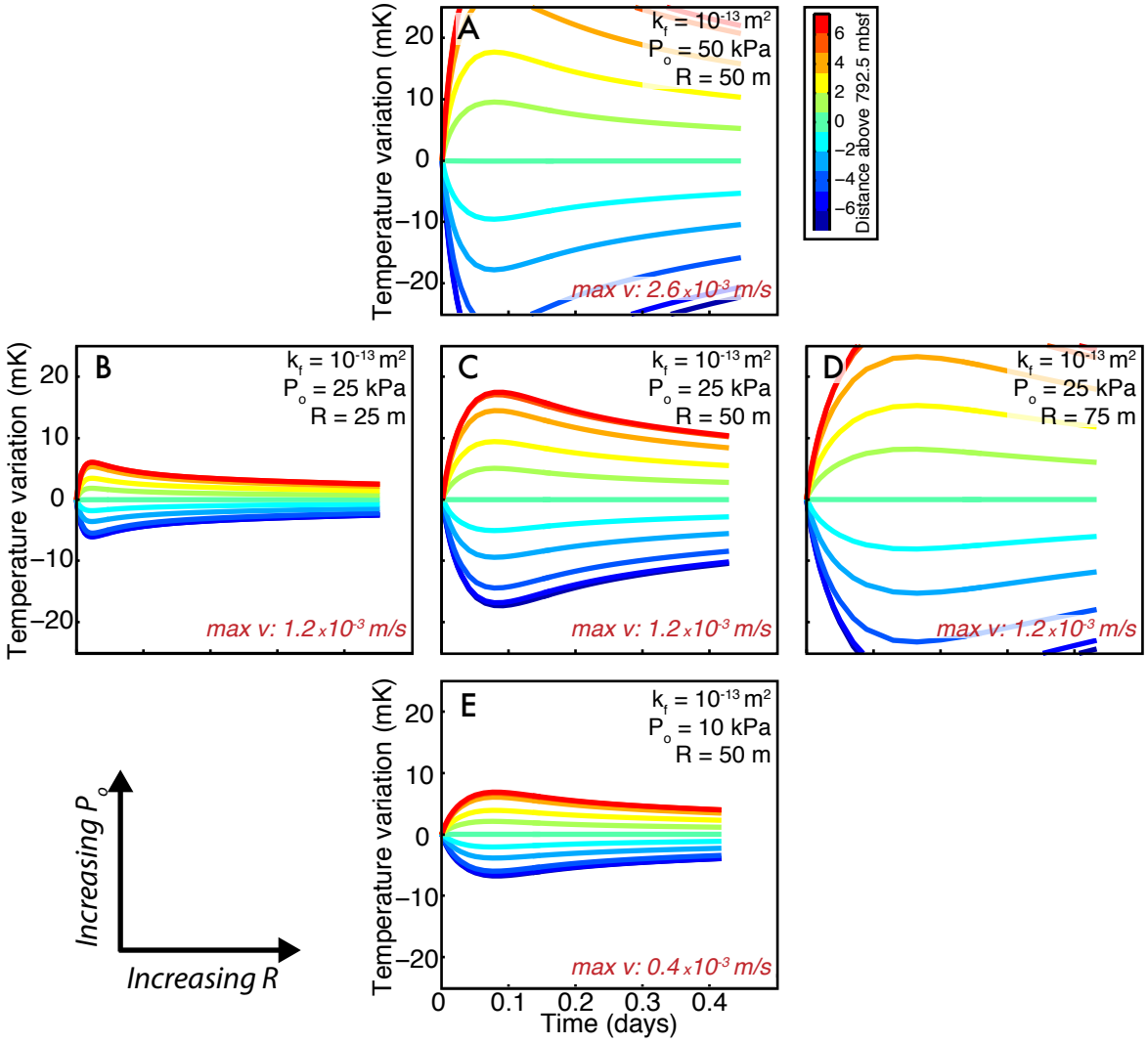

Figure DR7: Similar to Figure 4. Results of model simulations that together highlight the sensitivity of model parameterization choices on resulting temperature patterns. For the same fracture zone permeability, differences in either initial pressure Po or radial extent of the permeable zone R affect the resulting pattern but do not necessarily affect the peak fluid velocity, max v. Panel C is the same result as Figure 4A and Figure DR6A.

Table DR1: Earthquakes identified in nearby ocean bottom pressure data and whether or not they are associated with a fluid pulse.The direction of expected volumetric strain at the JFAST site is computed for earthquakes with NIED F-NET earthquake focal mechanisms.

TIME (GMT)	Fluid Pulse?	OBP Spike	Distance	Latitude	Longitude	Mw	Mj	MT Depth	JMA Depth	Volumentric Strain Direction
(GMT)	(1=Yes; 0=No)	(Pa)	(km)					(km)	(km)	(1=compression; -1=dilation)
14-Oct-2012 11:11:34	0	1837.1	49	38.284	144.259	5.3	5.4	5	46	1
25-Oct-2012 10:32:27	0	431.92	184	38.2893	141.8595	5.6	5.6	50	47.56	1
28-Oct-2012 03:04:09	0	967.02	6379	52.788	-132.101	7.8	-	14	-	
05-Nov-2012 04:30:26	1	1388.6	25	37.8467	143.6535	5.5	5.7	11	47	1
07-Nov-2012 16:35:47	0	174.74	11836	13.963	-91.854	7.4	-	24	-	
09-Nov-2012 03:51:53	0	196.26	253	36.8775	141.3795	5.2	5.5	5	32.5	1
11-Nov-2012 01:12:39	0	276.5	4836	23.005	95.885	6.8	-	13.7	-	
16-Nov-2012 08:25:54	0	166.73	374	35.357	141.2297	5.4	5.5	26	30.24	-1
16-Nov-2012 18:12:40	0	153.67	1562	49.28	155.425	6.5	-	29	-	
30-Nov-2012 11:42:54	0	135.3	144	39.2333	143.8538	4.8	4.9	8	27	1
07-Dec-2012 08:18:31	1	1.29E+05	38	37.8158	144.3153	7.3	7.4	11	46	-1
07-Dec-2012 08:31:10	1	14281	5	37.9198	143.8557	6.1	6.6	14	30	1
07-Dec-2012 12:05:24	1	1296.8	12	37.9052	143.7867	5.1	5	5	50	1
07-Dec-2012 16:01:51	1	475.87	19	37.798	143.7857	4.9	5	5	51	-1
07-Dec-2012 16:18:40	1	475.87	20	37.8057	143.7608	4.7	4.8	5	52	-1
07-Dec-2012 18:49:25	1	246.08	6	37.929	143.841	-	4.4	-	46	
07-Dec-2012 20:30:39	1	254.52	32	37.9518	143.5542	4.7	4.7	5	35	1
07-Dec-2012 23:00:00	1	822.55	23	37.8143	143.7095	5.1	5.2	5	44	-1
08-Dec-2012 07:18:10	1	407.98	12	37.9903	143.7913	4.4	4.6	5	42	1
08-Dec-2012 12:50:07	1	168.17	39	37.6887	143.6038	4.5	4.6	5	50	1
08-Dec-2012 13:53:36	1	281.05	8	37.8665	143.8883	4.6	4.7	5	45	-1
08-Dec-2012 19:21:10	1	109.66	9	37.9613	143.8175	4	4.3	5	30	-1
09-Dec-2012 02:34:17	1	1204.1	31	37.8753	143.5665	5.1	5.2	5	42	1
09-Dec-2012 05:29:08	1	249.64	5	37.9627	143.8675	4	3.8	5	46	-1
09-Dec-2012 10:13:39	1	114.86	15	38.0758	143.9332	4.3	4.6	5	41	-1
09-Dec-2012 11:47:01	1	143.81	32	38.2093	143.7992	4.6	4.7	11	39	-1

TIME (GMT)	Fluid Pulse?	OBP Spike	Distance	Latitude	Longitude	Mw	Mj	MT Depth	JMA Depth	Volumentric Strain Direction
09-Dec-2012 14:42:16	1	679.18	11	37.8448	143.8978	4.8	4.8	5	50	-1
09-Dec-2012 18:59:46	1	2853.1	14	38.0203	143.7962	4.7	4.7	5	45	-1
09-Dec-2012 23:50:33	1	529.71	38	37.6838	143.6198	4.8	5	5	23	-1
10-Dec-2012 00:09:50	1	412.93	37	37.6453	143.7235	4.7	4.7	5	46	-1
10-Dec-2012 09:09:31	0	707.77	26	37.876	143.6333	4.9	4.8	5	43	1
10-Dec-2012 16:53:09	1	180.55	5158	-6.533	129.825	7.1	-	155	-	
10-Dec-2012 22:08:01	1	397.39	24	37.7732	143.7403	4.9	4.9	5	50	-1
10-Dec-2012 23:17:41	1	143.25	26	37.7383	143.765	4.3	4.2	5	50	1
14-Dec-2012 01:22:02	1	267.87	49	37.586	143.5837	4.8	4.8	5	45	-1
15-Dec-2012 10:55:22	1	132.57	34	37.6963	143.6713	4.7	4.7	8	53	-1
17-Dec-2012 22:52:18	0	273.47	30	37.8023	143.6178	4.8	4.7	5	46	1
20-Dec-2012 03:17:04	0	153.59	46	37.6047	143.6045	4.6	4.9	5	46	-1
20-Dec-2012 09:31:38	1	1261	8	37.9948	143.8568	4.5	4.7	5	41	-1
29-Dec-2012 14:59:37	0	239.23	173	38.7173	142.1962	5.5	5.5	44	40.98	1
31-Dec-2012 09:35:58	0	198.53	37	37.6445	143.7157	4.5	4.7	5	55	-1
02-Jan-2013 21:50:47	0	135.77	43	37.6122	143.6577	4.6	4.7	5	52	-1
05-Jan-2013 08:58:19	0	1552.3	6125	55.394	-134.65	7.5	-	10	-	
08-Jan-2013 07:51:30	0	170.32	274	40.1197	142.4392	5.5	5.4	38	34.22	1
02-Feb-2013 14:17:36	0	2565.1	532	42.6892	143.2362	6.9	6.5	116	107.65	-1
06-Feb-2013 01:23:20	0	934.59	5894	-11.2541	164.9323	7.1	-	10.14	-	
07-Feb-2013 18:59:16	0	515.35	5897	-11.001	165.658	6.7	-	10	-	
08-Feb-2013 11:12:13	0	488.83	5896	-10.905	165.886	6.8	-	15.9	-	
08-Feb-2013 15:26:38	0	657.93	5904	-10.932	166.021	7.1	-	21	-	
09-Feb-2013 21:02:23	0	229.8	5899	-10.952	165.838	6.6	-	15.6	-	
13-Feb-2013 19:52:41	0	105.34	24	37.7937	143.7107	4.3	4.4	5	38	1
14-Feb-2013 13:13:53	0	448.25	3299	67.582	142.564	6.6	-	9.9	-	
19-Feb-2013 12:27:35	1	234.8	377	35.3458	141.1988	5.4	5.6	29	37.21	-1
25-Feb-2013 07:23:54	1	768.9	415	36.8737	139.4128	5.8	6.3	8	2.84	1

TIME (GMT)	Fluid Pulse?	OBP Spike	Distance	Latitude	Longitude	Mw	Mj	MT Depth	JMA Depth	Volumentric Strain Direction
28-Feb-2013 14:05:50	0	200.63	1791	50.942	157.339	6.9	-	41	-	
01-Mar-2013 12:53:52	1	217.81	1799	50.938	157.511	6.4	-	40.9	-	
24-Mar-2013 04:18:34	0	200.43	1914	50.731	160.159	5.9	-	8	-	
01-Apr-2013 18:53:16	0	1194	178	39.5053	143.5183	6	6.2	20	28.72	1
02-Apr-2013 02:08:45	0	335.28	176	39.4985	143.6003	5.5	5.7	17	27	1
05-Apr-2013 21:53:00	0	144.84	64	37.4812	144.3628	4.5	4.7	5	51	1
06-Apr-2013 04:42:36	0	143.99	4645	-3.513	138.477	7	-	66	-	
12-Apr-2013 20:33:18	1	339.54	904	34.4188	134.829	5.8	6.3	11	14.85	-1
14-Apr-2013 13:25:02	0	168.47	225	37.5327	141.406	5.4	5.3	53	51.01	1
16-Apr-2013 10:44:21	0	465.79	7471	28.107	62.053	7.7	-	82	-	
17-Apr-2013 08:57:34	1	452.8	596	34.0473	139.353	5.8	6.2	8	9.37	1
17-Apr-2013 12:03:32	1	1438	209	38.461	141.6197	5.9	5.9	59	57.79	1
19-Apr-2013 03:05:55	1	885.9	1006	45.3008	150.9572	7.2	7	98	125	1
19-Apr-2013 19:59:26	0	316.97	196	39.6573	143.4268	4.4	4.6	20	24.63	1
20-Apr-2013 00:02:47	0	782	3840	30.308	102.888	6.6	-	14	-	
20-Apr-2013 13:12:51	0	224.37	1714	50.105	157.165	6.1	-	18	-	
21-Apr-2013 03:22:14	0	245.63	986	29.9022	139.4075	6	6.4	400	447.46	-1